



TECHNICAL ARTICLE

Microstructural Evolution and Strengthening Behavior of High-Pressure Die-Cast High-Cu Al-Si-Cu-Mg Alloy with T5 Treatment

G.S. Peng , X.Y. Fu, Y.C. Gu, G.S. Song, S.S. Chen, Q.Q. Sun, and W.D. Hua

Submitted: 16 September 2021 / Revised: 16 December 2021 / Accepted: 2 January 2022 / Published online: 11 February 2022

Conventional high-pressure die casts (HPDC) cannot be solution-treated at high temperature owing to the presence of air or gas in the alloy that may lead to the formation of undesired surface blistering. HPDC Al castings are typically subjected to T5 aging treatment (direct artificial aging after casting) to improve the mechanical properties. In this study, microstructural evolution and strengthening behavior of an HPDC Al-Si-Cu-Mg alloy with high Cu content aged by T5 treatment were investigated using electrical conductivity, hardness, and tensile tests combined with differential scanning calorimetry, x-ray diffraction, and scanning transmission electron microscopy characterization. Numerous dislocation tangles and nano-sized Si particles were observed in the HPDC Al castings. Most Cu dissolved into the Al matrix. An increase in hardness and electrical conductivity during the peak-aging treatment was attributed to formation of Guinier–Preston zones. Most dislocation tangles and nano-sized Si particles disappeared during further aging and Al₂Cu precipitates formed, which led to a slight decrease in hardness and increase in electrical conductivity. The strengthening mechanism of over-aged HPDC alloys is attributed to precipitation of the equilibrium Al₂Cu phase. HPDC alloys subjected to T5 aging treatment (175 °C for 420 min) exhibited the best mechanical properties: ultimate tensile strength, yield strength, and elongation reached 293 MPa, 212 MPa, and 3.1%, respectively.

Keywords Al-Si-Cu-Mg, dislocation, high-pressure die cast, precipitation, T5 aging

1. Introduction

There has been increased demand for Al alloys in recent decades owing to their applications in the aerospace and transportation industries. Compared with other forming technologies, high-pressure die-casting (HPDC) possesses many merits, such as ease of mass production, good surface finish, dimensional accuracy, and the ability to form complex components. Almost 50% of Al castings are fabricated by an HPDC process (Ref 1, 2). A T6 or T7 heat treatment, which comprises high-temperature solution treatment and artificial aging, is an important way to develop die-cast alloys with high yield strength and acceptable elongation (Ref 3). Unfortunately, high-temperature solution heat treatment cannot be applied to Al castings produced by conventional HPDC, owing to the

blistering and dimensional instability that occurs on the surface of the castings (Ref 4–6). To minimize detrimental effects that occur during solution heat treatment, vacuum (or ultra-vacuum) HPDC processes were developed to lessen gas entrapment and hence minimize blistering (Ref 7, 8), but low production efficiency and high cost limit the widespread application of these technologies. Although it is reported that low-temperature solution treatment and a short solution treatment time can achieve an adequate supersaturated solid solution without blistering (Ref 9–12), some risk of blistering still exists, especially for thin HPDC Al castings.

T5 aging treatment (direct artificial aging after casting) is desired to improve the mechanical properties of HPDC Al castings; however, only limited work has been reported on this system and controversy still exists concerning the evolution of hardening precipitates during the T5 aging treatment. Nakata et al. (Ref 13) attributed the good strength of Al-7Si-0.5Mg-0.01Sr to fine and uniform β precipitates. Inoue et al. (Ref 14) found the formation of clusters during pre-aging of Al-9Si-0.3Mg. Ando et al. (Ref 15) claimed that Si compounds precipitated during preliminary aging and Al-Cu compounds precipitated later at low aging temperature in Al-11Si-1.8Cu-0.2Mg. Mishra et al. (Ref 16) reported that the S' phase formed first and then partially dissolved as Si in an Al-Si-Cu-Mg alloy. In contrast, an investigation of precipitation in Al-Si-Cu-Mg alloys for HPDC castings showed that precipitation hardening did not occur in T5-treated materials, but did occur in T6-treated material, in which strengthening was caused by precipitation of the S'' phase (Ref 17).

In this work, an extensive study was carried out to clarify the T5-aging strengthening behavior of an HPDC Al-Si-Cu-Mg

G.S. Peng, X.Y. Fu, Y.C. Gu, G.S. Song, and S.S. Chen, Key Laboratory of Green Manufacturing and Surface Technology of Advanced Metal Materials, Ministry of Education, School of Materials Science and Engineering, Anhui University of Technology, Ma'anshan 243002, People's Republic of China; Q.Q. Sun, School of Materials, Sun Yat-sen University, Guangzhou 510006, People's Republic of China; and W.D. Hua, Gangyan Co. Ltd, Jiangsu 225300, People's Republic of China. Contact e-mails: pengguosheng@126.com and sunqq7@mail.sysu.edu.cn.

alloy with high Cu content. Evolution of microstructural properties, such as dislocations, precipitates, and behavior of the Cu solute, were examined as a function of aging time at 175 °C. The results of this study can improve understanding of the relationship between microstructure and mechanical properties of T5-aged HPDC Al alloys.

2. Material and Experimental Procedure

The alloy compositions are shown in Table 1. Die casting was conducted using a cold-chamber die-cast machine (DC-350J-MS model, Toshiba) with a locking force of 3500 kN. The melt was held at 700 °C and cast into a mold. The die mold, HPDC Al castings, and specimens for tensile tests are shown in Fig. 1(a)-(c), respectively. The temperature of the mold, plunger speed, gate speed, and casting pressure were 170 °C, 0.25 m/s, 0.9 m/s, and 60 MPa, respectively. The cast samples were held in the mold for 20 s and then quenched in air. The as-cast HPDC alloys were artificially aged at 175 °C and samples taken at different times for characterization.

The variation in hardness during aging treatment was determined using specimens polished by SiC paper and then measured using a Brinell hardness tester. At least five points were measured for each condition and average values are reported. Average values of electrical conductivity were determined by measuring at least five areas of a sample using an FQR7501A digital micrometer. Tensile properties were determined by machining dog-bone-shaped samples of 2 mm gauge thickness, 6 mm gauge width, and 25 mm gauge length, and testing these using an Instron 3369 materials testing machine at a displacement rate of 2 mm min⁻¹. At least three tensile tests were conducted for each condition.

A Zeiss reflected-light optical microscope was used for characterization of optical microstructures. Differential scanning calorimetry (DSC; 409PC, Netzsch,) was carried out to analyze the evolution of precipitates using a heating rate of 5 °C/min. X-ray diffraction (XRD; D8ADVANCE, Bruker) was used to identify phases and evaluate the dislocation density according to the full-width at half maximum (FWHM) of the α -Al peak using a CuK₂ radiation source (45 kV, step size = 2°/min, 2° ≤ 2θ ≤ 100°). It is well known that FWHM reflects the dislocation density and that an increase in peak broadening can mainly be attributed to an increase in dislocations of a material based on XRD characterization (Ref 18, 19). The dislocation density (ρ) of alloys can be calculated using the relationship (Ref 20, 21):

$$\rho = \frac{2\sqrt{3}\langle \varepsilon^2 \rangle^{1/2}}{Db} \quad (\text{Eq 1})$$

where $\langle \varepsilon^2 \rangle^{1/2}$ is the root mean square microstrain, D is the coherent domain size, and b is the Burger's vector. Here $b = 0.285$ nm (Ref 22). ε and D were, respectively, estimated from

Table 1 Chemical composition of the investigated alloys in wt. %

Elements	Si	Cu	Mg	Fe	Mn	Zn	Al
Composition	14.61	4.44	0.43	0.71	0.17	0.51	Bal.

the slope and intercept of a linear equation obtained by fitting the XRD data using *Jade* software.

To prepare thin foils for scanning transmission electron microscopy (STEM) examination, slices cut from HPDC samples were mechanically ground and cut into 3-mm-diameter disks. These disks were ground to a thickness of less than 70 nm and ion-beam thinned on a Gatan precision ion-polishing system at a voltage of 5.0 kV and incident angle of 4°-6°. An FEI Talos F200X transmission electron microscope operating at 200 kV was used for STEM imaging, select area-diffraction pattern (SADP) analysis, and energy-dispersive x-ray spectroscopy (EDX) mapping analysis.

3. Results and Discussion

3.1 Microstructure Characterization

Figure 2 shows a typical as-polished microstructure of the die-cast AlSi14Cu4MgZn alloy. As expected, numerous primary Si and Al-Si eutectic phases are observed in the alloys in Fig. 2(a)-(b). With reference to the Al-Si phase diagram (Ref 23), as solidification proceeds, the primary Si phase is first solidified followed by the Al-Si eutectic phases. Figure 2(b) shows that compact Fe-rich phases are apparent: these are termed 'sludge' in the die-casting industry and are modified by Mn as an alloying element (Ref 24). In addition, some coarse gray Cu-rich phase can be seen, which may result from the high Cu content, present as an alloying element. Furthermore, two typical α -Al grain structures can be seen in Fig. 2(b): coarse α_1 -Al grains solidified in the shot sleeve at lower cooling rate and fine secondary α_2 -Al grains solidified in the die cavity at higher cooling rate (Ref 25).

To investigate the precipitation behavior during heating of HPDC alloys, the DSC curves for these alloys were compared with those of similar composition but prepared via gravity casting (GC) using a steel die. The results are shown in Fig. 3. For the GC alloys, a single exothermic peak (I) appeared at 75 °C, which may correspond to the formation of Guinier-Preston (GP) zones containing Cu. In comparison, the HPDC alloys exhibited two additional exothermic peaks and one endothermic peak, occurring at approximately 125, 175, and 250 °C, respectively. In HPDC alloys, the reason for the occurrence of exothermic peak I is similar to that of GC alloys. The peak I area of the HPDC alloy was larger than that of the GC alloy, indicating a corresponding larger volume fraction of the GP zone. Exothermic peaks II and III may be attributed to precipitation of θ' and θ phases, respectively. This DSC analysis of peak position and assignment is consistent with the work of Xiong et al. (Ref 26). It should be noted that no obvious dissolution endotherm was detected between exotherms I and II, indicating that GP zones associated with exotherm I serve as precursors for nucleating the complex higher-order θ' phase. In addition, endotherm IV of HPDC may correspond to dissolution of the ($\theta' + \theta$) phase. The difference in precipitation behavior between the GC and HPDC alloys is attributed to the difference in cooling rate: HPDC exhibits a faster cooling rate (typically 100-1000 °C/s) (Ref 27-29), which contributes to a short die-filling time and thin walls. The fast cooling rate of HPDC alloys leads to more defects (e.g., dislocations) and a higher Cu solute content in the Al matrix. In addition, exothermic peaks II and III of HPDC alloys

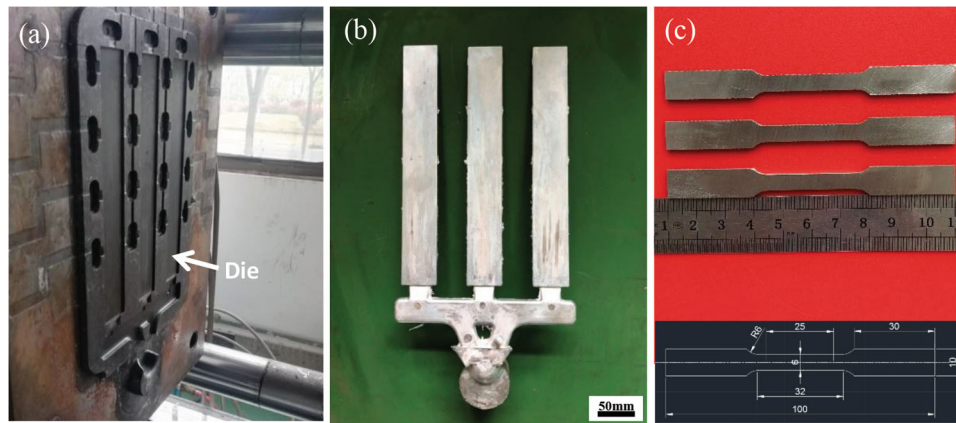


Fig. 1 Schematic diagram for specimen preparation (a) die mold for HPDC; (b) HPDC Al castings; (c) specimen for tensile test

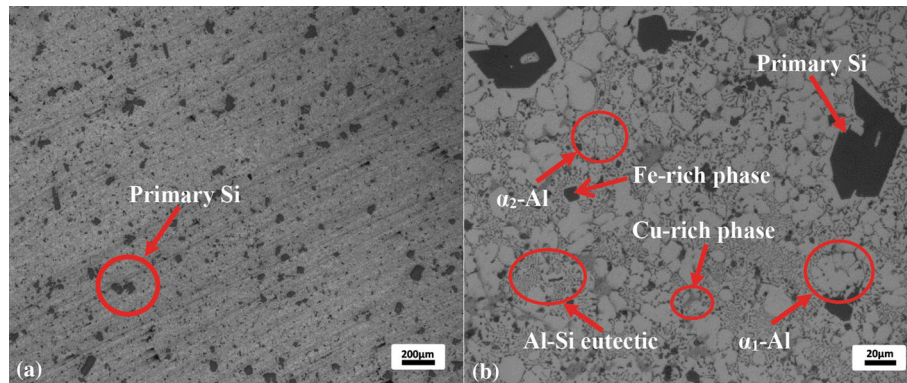


Fig. 2 Typical microstructures of die-cast AlSi14Cu4MgZn alloy (a) Low magnification; (b) High magnification

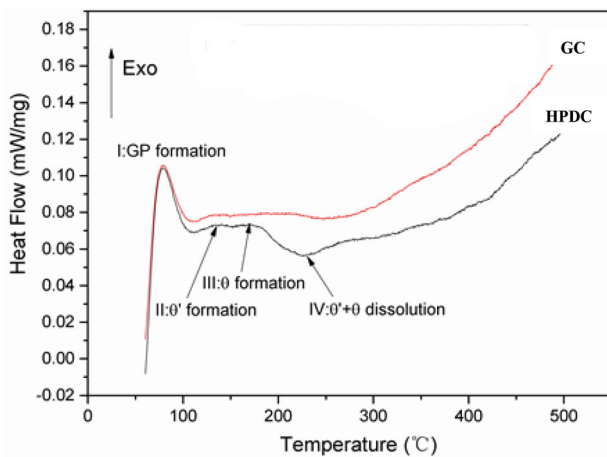


Fig. 3 DSC analysis of samples prepared by gravity casting and HPDC

are less obvious than those of alloys that are subjected to high-temperature solution followed by water quenching, suggesting that supersaturated solute content (which mainly refers to the Cu solute in this study) in HPDC that is treated only by air quenching is lower than that of alloys treated by both solutioning and water quenching (Ref 30).

Figure 4 shows XRD spectra of the GC and HPDC alloys and the classical Williamson–Hall plot of the corresponding FWHM. Both alloys exhibited peaks attributed to the α -Al and

Si phases. In addition, the GC alloy showed distinct Al_2Cu peaks, suggesting that this contained more Al_2Cu phase than HPDC. The faster cooling rate of HPDC helps more Cu atoms to remain in the Al matrix and retards Cu atoms from forming the coarse Al_2Cu phase. Furthermore, all α -Al peaks of the HPDC alloy shifted toward lower 2θ value compared with those of the GC alloy, which may contribute to residual stress resulting from the fast cooling of HPDC (Ref 31, 32). The classical Williamson–Hall plot of the FWHM from XRD characterization is shown in Fig. 4(b). The calculated dislocation densities of the HPDC and GC alloys are $1.6 \times 10^{15} \text{ m}^{-2}$ and $1.7 \times 10^{14} \text{ m}^{-2}$, respectively. It should be noted that the HPDC alloy had an order-of-magnitude higher dislocation density. HPDC alloy exhibits large thermal stress due to its fast cooling rate, so plastic strain occurs in the α -Al matrix to relax this stress, resulting in a high dislocation density. Both the higher dislocation density and higher Cu solute content lead to different precipitation behavior of HPDC alloys compared with that of GC alloys during T5 aging treatment. This was further investigated using more advanced characterization methods.

3.2 Strengthening Behavior during T5 Aging Treatment

To investigate the influence of T5 aging hardening behavior on the variation in hardness and electrical conductivity, Brinell hardness and electrical conductivity measurements were carried out. Figure 5 shows the variation in these two parameters during the T5-aging treatment. Electrical conductivity increased with time, whereas hardness first increased and then slightly

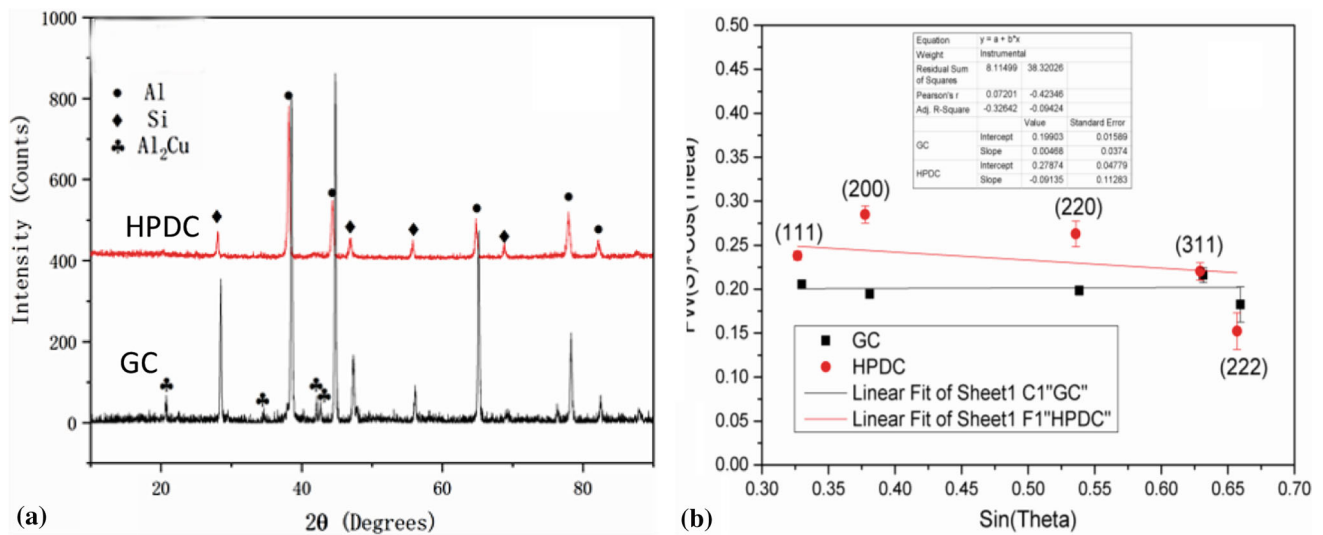


Fig. 4 XRD analysis of samples prepared by GC and HPDC (a) and the classical Williamson-Hall plot of the FWHM from XRD characterization (b)

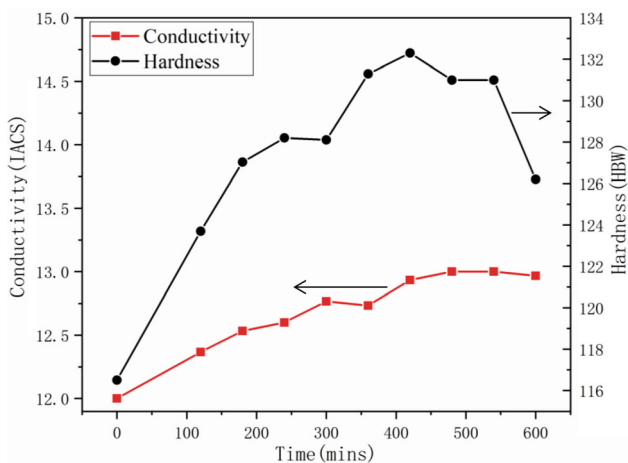


Fig. 5 The variation in hardness and electric conductivity as a function of aging time at 175 °C

decreased with aging time. With increased aging time, more solute (Cu) precipitated from the Al matrix and lessened distortion of the matrix. This resulted in a continuous increase in electrical conductivity. The variation of hardness reflects precipitation of the solute element, corresponding to peak-aging (initial increase) and then over-aging (slight decrease). When the T5-aging time reached 420 min, the corresponding hardness value was highest, at 133 HBW.

Figure 6 shows the mechanical properties of the HPDC alloy for different aging times during T5 treatment. Alloys aged for 7 h at 175 °C showed the highest ultimate strength, yield strength, and elongation of 293 MPa, 212 MPa, and 3.1%, respectively. These values were 30, 32, and 24% higher, respectively, than the corresponding values measured for the as-cast HPDC alloy. On further prolonging the aging time to 10 h, the ultimate strength, yield strength, and elongation slightly decreased. This variation of mechanical properties is consistent with that of hardness as a function of aging time.

3.3 Microstructural Evolution during T5 aging Treatment

Figure 7 shows STEM images viewed along the $[-112]$ crystal zone axis and corresponding EDX mapping analysis of as-cast HPDC alloys. These alloys contained an abundance of dislocations, which is consistent with XRD characterization (Fig. 4). In addition to the primary Si and eutectic Si phases shown in Fig. 2, numerous nanoscale Si particles (40-60 nm) are also seen in Fig. 7(b) and (d), associated with many dislocation tangles. It can be assumed that nucleation of nanoscale Si particles on the dislocations readily occurred because this contributes to reducing the total strain energy of the Si embryo and total free energy of the material. The EDX mapping analysis shown in Fig. 7(e) and (f) indicates that most Cu and Mg dissolved into the Al matrix and were evenly distributed throughout the sample.

When the as-cast HPDC alloy was held at 175 °C (T5 aging treatment), the hardness increased with time and reached peak-aging after 420 min. The corresponding STEM image viewed along the $[100]$ crystal zone axis and EDX mapping are shown in Fig. 8. The microstructure of the peak-aged HPDC alloy was similar to that of the as-cast HPDC alloy and still contained a high dislocation density and nano-sized Si particles, as shown in Fig. 8(a)-(c). However, the contrast of nano-sized Si particles in the peak-aged HPDC alloy was weaker than that of the as-cast HPDC alloy, indicating that Si atoms from the nanoscale Si particles diffused into the Al matrix to some extent during the aging treatment (Fig. 8e). In addition, the Cu distribution seemed to be more segregated than that of as-cast HPDC alloys, which most likely corresponded to GP zones. The diffraction pattern confirmed the existence of GP zones, where distinct discontinuous streaks parallel to the $\langle 100 \rangle_{\alpha}$ direction through $\{200\}$ spots were observed (Ref 33). These streaks contributed to the elastic strain field from coherent GP zones. It is understandable that dissolved Cu atoms readily moved toward the dislocations as aging proceeded because segregation of Cu atoms along the dislocations can effectively decrease the interfacial energy of dislocations with the Al matrix. In fact, these phenomena are well studied in Al-Cu alloys, where deformation prior to aging can increase dislocation density, and thereby the number of nucleation sites for heterogeneous

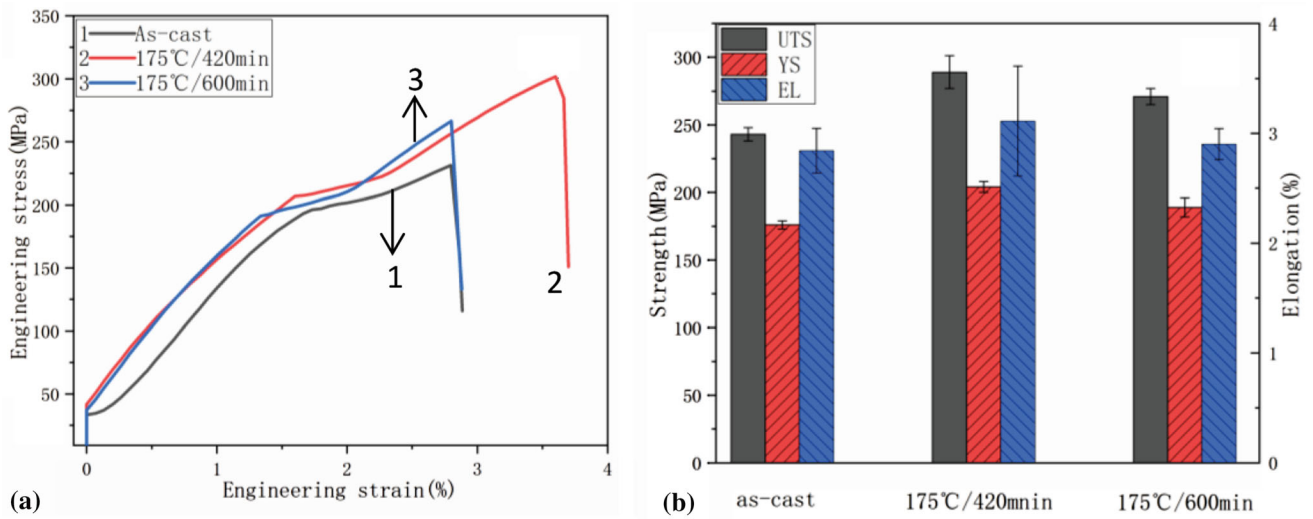


Fig. 6 Tensile properties of the as-cast, peak-aging and over-aging HPDC alloys. (a) Typical tensile-strain curves; (b) average tensile properties of HPDC alloys

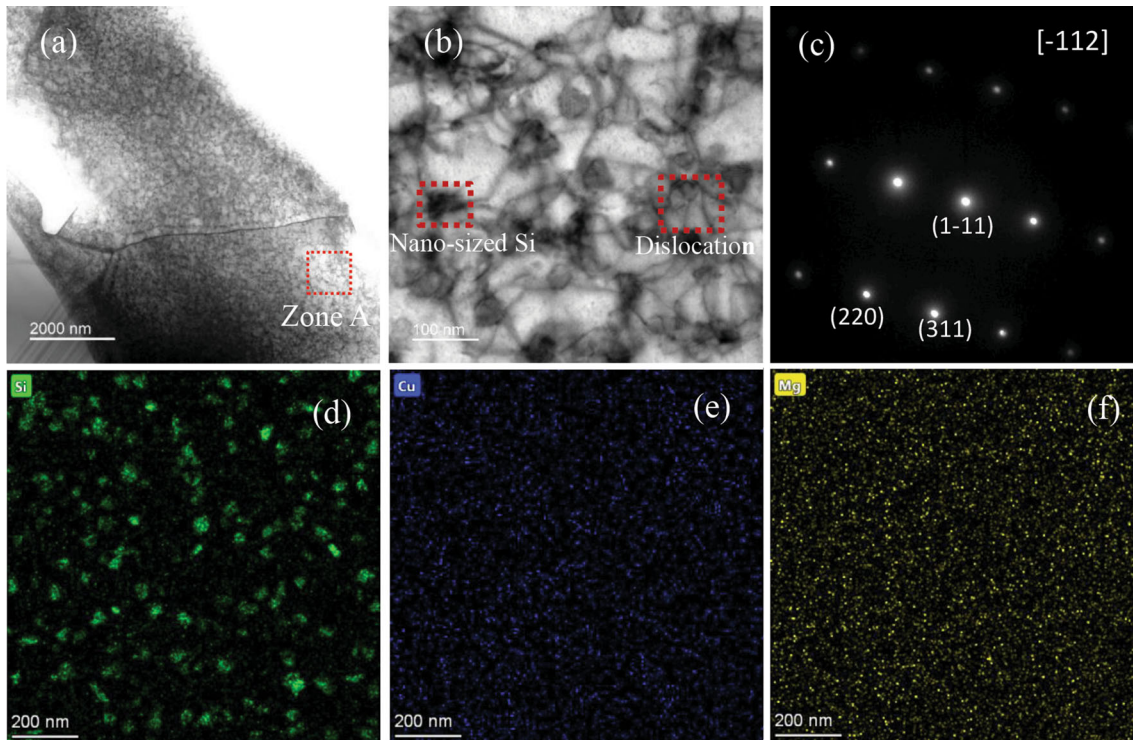


Fig. 7 STEM image and corresponding mapping EDX from as-cast HPDC alloys (a) low magnification; (b) high magnification from Zone A; (c) SAED pattern; (d) Si mapping; (e) Cu mapping; (f) Mg mapping

precipitation, by accelerating the diffusion of Cu atoms (Ref 34-36). DSC characterization of the HPDC alloys also confirmed the formation of GP zones containing Cu, as shown in Fig. 3. The combined effects of high dislocation density, nanoscale Si particles, and coherent GP zones contributed to the highest hardness value for the peak-aged HPDC alloy.

With further prolonging of aging time, the hardness slightly decreased whereas the electrical conductivity continued to increase. This stage is defined as over-aging. An STEM image viewed along the [110] crystal zone axis and corresponding EDX mapping are shown in Fig. 9 and 10, respectively. The

microstructure of the over-aged HPDC alloy differed obviously from those of the as-cast and peak-aged HPDC alloys: the nano-sized Si particles had fully dissolved into the Al matrix by diffusion and the dislocations had completely disappeared owing to the static recovery effect. Instead, a needle-like phase with a high number density was observed. An EDX map (Fig. 10) of this phase showed that it contained mainly Cu. A well-accepted precipitation sequence for Al-Si-Cu-Mg alloys with high Cu/Mg ratio has been proposed as follows: supersaturated solid solution \rightarrow GP I (Cu/Al-rich) \rightarrow metastable θ' \rightarrow equilibrium θ (Ref 37, 38). Therefore,

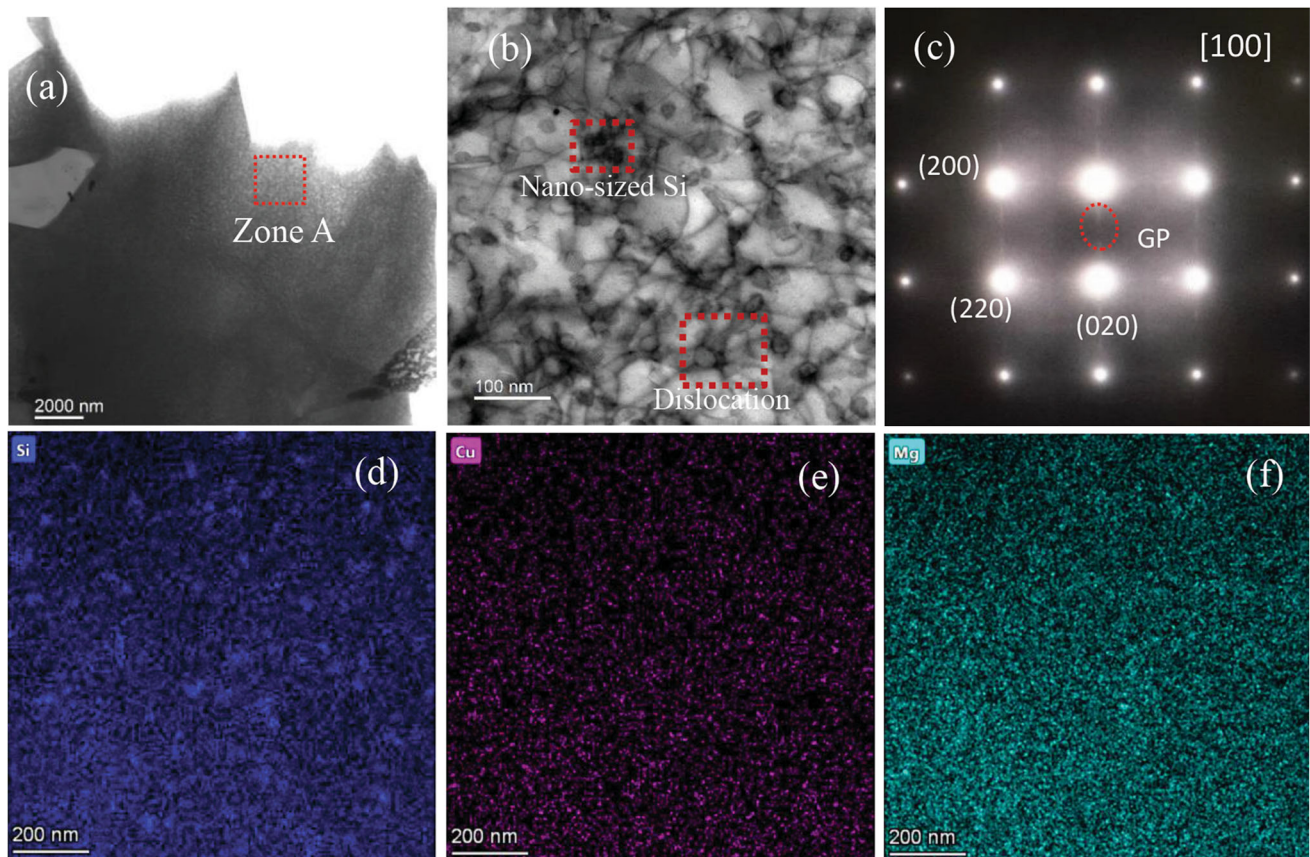


Fig. 8 STEM image and corresponding mapping EDX from as-peak HPDC alloys (a) low magnification; (b) high magnification from Zone A; (c) SAED pattern (d) Si mapping; (e) Cu mapping; (f) Mg mapping

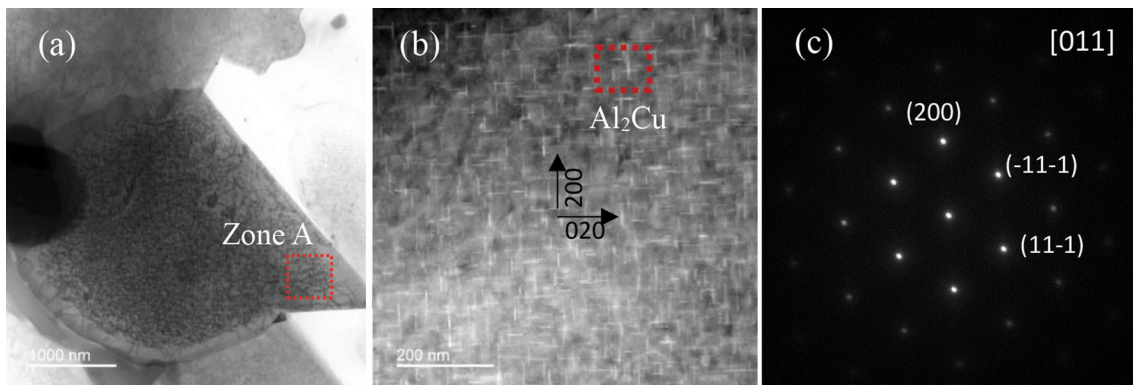


Fig. 9 STEM image from over-aging HPDC alloys (a) low magnification; (b) high magnification from Zone A; (c) SAED pattern

considering the alloy's composition and high Cu content and previous studies of the precipitation of Al-Cu alloys, the needle-like phase is most likely the Al_2Cu phase (Ref 39-42). The Al_2Cu phase is an equilibrium phase at this stage and has no coherent relationship with the Al matrix, so no diffraction streaks from precipitates are observed in Fig. 9(c). The disappearance of both dislocations and nano-sized Si particles decreased the hardness, while precipitation of the Al_2Cu phase increased the hardness. Considering these two offsetting effects, the overall hardness value slightly decreased when

compared with that of the peak-aged alloy. In addition, precipitation of the semi- or non-coherent Al_2Cu phase further lessened the Al lattice distortion and thereby increased the electrical conductivity.

Figure 11 summarizes the microstructure evolution envisioned for HPDC alloys with a high Cu content during T5 aging treatment. As characterized by DSC, XRD, and STEM analyses, as-cast HPDC Al alloys contain an abundance of dislocations and nano-sized Si particles as well as well-distributed Cu solute. When the alloy is aged at 175 °C, Cu

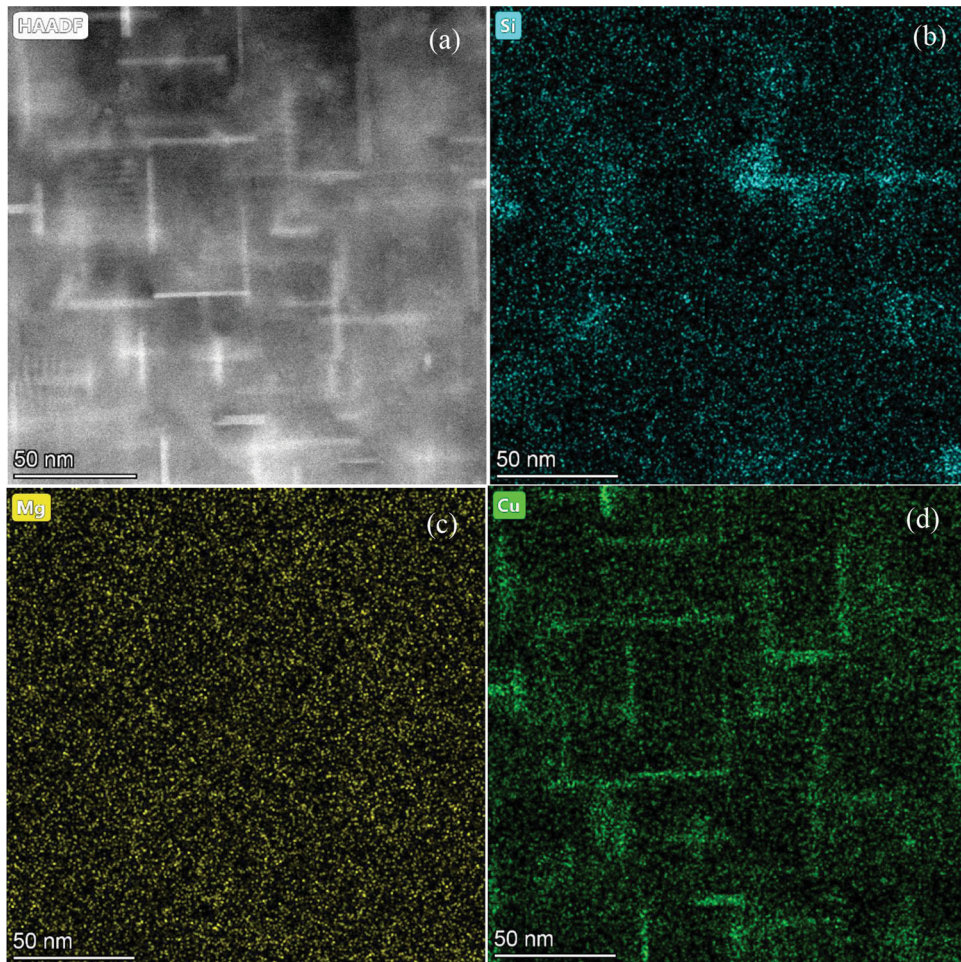


Fig. 10 STEM image and corresponding mapping EDX from over-aging HPDC alloys (a) STEM image; (c) Si mapping; (d) Mg mapping; (e) Cu mapping

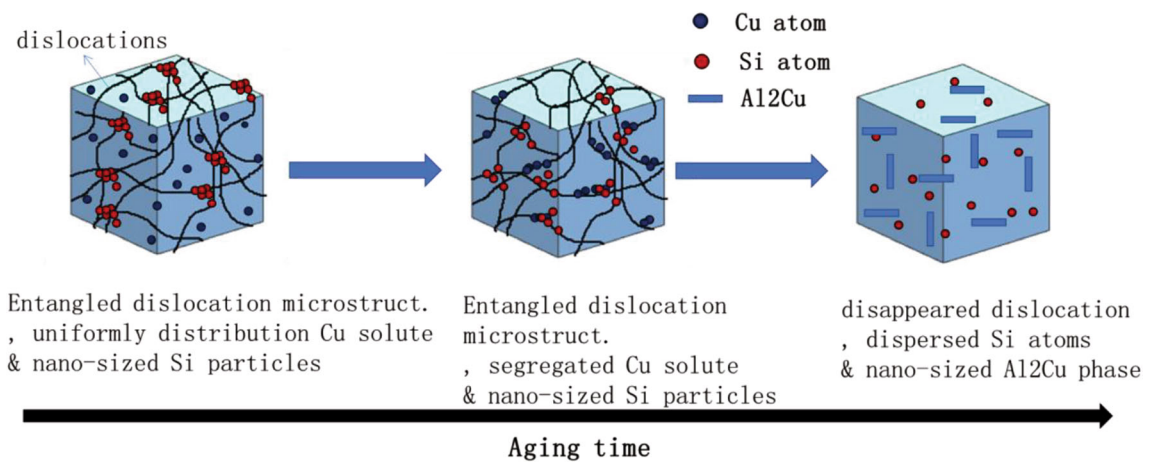


Fig. 11 Schematic representation of the microstructure evolution envisioned for HPDC alloys containing high Cu content during T5 aging treatment

segregates close to dislocation tangles and formed GP zones, which are responsible for the high hardness and mechanical properties. On longer aging time, GP zones are transformed into needle-like equilibrium Al_2Cu phases and the nano-sized

Si particles and dislocations largely disappear, which corresponds to a slight decrease in hardness and mechanical properties.

4. Conclusions

Microstructural evolution and strengthening behavior of an HPDC Al-Si-Cu-Mg alloy with a high Cu content aged by T5 treatment was investigated. The following conclusions can be drawn:

- (1) For HPDC Al castings, an abundance of dislocation tangles and nano-sized Si particles were observed and the Cu alloying element was dissolved in the Al matrix.
- (2) For peak-aged HPDC Al castings, the Cu solute segregated to nearby dislocation tangles and formed GP zones, to which the strength improvement is attributed.
- (3) For over-aged HPDC Al castings, microstructural evolution of T5-treated HPDC alloys reflected the disappearance of both dislocation tangles and nanoscale Si particles, and precipitation of the equilibrium Al_2Cu phase, which caused a decrease in strength.
- (4) The over-aged strengthening mechanism of T5-treated HPDC alloys is attributed to precipitation of the equilibrium Al_2Cu phase.
- (5) HPDC alloys exhibited the best mechanical properties when subjected to the T5 aging treatment (175 °C for 420 min): the ultimate tensile strength, yield strength, and elongation reached 293 MPa, 212 MPa, and 3.1%, respectively.

Acknowledgments

This study was financially supported by the Anhui Provincial Natural Science Foundation (1808085ME123, 1908085MF197), the Projects of International Cooperation and Exchanges in Anhui Provincial Key Project of Research and Development Plan (1804b06020363, 202004b11020010), Natural Science Foundation of Anhui Provincial Education Department (Grant No. KJ2020A0262).

Conflict of interest

On behalf of all authors, the corresponding author states that there is no conflict of interest.

References

1. F. Bonollo, N. Gramegna and G. Timelli, High-pressure Die-casting: Contradictions and Challenges, *JOM*, 2015, **67**, p 901–908. <https://doi.org/10.1007/s11837-015-1333-8>
2. L. Wang, M. Makhlof and D. Apelian, Aluminium Die Casting Alloys: Alloy Composition, Microstructure, and Properties-performance Relationships, *Int. Mater. Rev.*, 1995, **40**, p 221–238. <https://doi.org/10.1179/imr.1995.40.6.221>
3. X.X. Dong, H.Z. Youssef, Y.J. Zhang, H.L. Yang, S.H. Wang and S.X. Ji, Advanced Heat Treated Die-cast Aluminium Composites Fabricated by TiB_2 Nanoparticle Implantation, *Mater. Design*, 2020, **186**, 108372. <https://doi.org/10.1016/j.matdes.2019.108372>
4. E.J. Vinarcik, *High integrity die casting processes*, Wiley, New York, 2003
5. L.H. Wang, P. Turnley and G. Savage, Gas Content in High Pressure Die Castings, *J. Mater. Process. Technol.*, 2011, **211**, p 1510–1515. <https://doi.org/10.1016/j.jmatprotec.2011.03.024>
6. H. Toda, P.C. Qu, S. Ito, K. Shimizu, K. Uesugi, A. Takeuchi, Y. Suzuki and M. Kobayashi, Formation Behaviour of Blister in Cast

- Aluminium Alloy, *Inter. J. Cast Metal. Res.*, 2014, **27**, p 369–377. <https://doi.org/10.1179/1743133614Y.0000000123>
7. H.J. Kang, P.H. Yoon, G.H. Lee, J.Y. Park, B.J. Jung, J.Y. Lee, C.U. Lee, E.S. Kim and Y.S. Choi, Evaluation of the Gas Porosity and Mechanical Properties of Vacuum Assisted Pore-free Die-cast Al-Si-Cu Alloy, *Vacuum*, 2021, **184**, 109917. <https://doi.org/10.1016/j.vacuum.2020.109917>
8. H.X. Cao, C.C. Wang, Q.Y. Shan, J.Q. Che, Z.W. Luo, L.H. Wang and M.T. Huang, Kinetic Analysis of Pore Formation in Die-cast Metals and Influence of Absolute Pressure on Porosity, *Vacuum*, 2019, **168**, 108828. <https://doi.org/10.1016/j.vacuum.2019.108828>
9. O. Ozhoga-Maslovskaja, E. Gariboldi and J.N. Lemke, Conditions for Blister Formation during Thermal Cycles of Al-Si-Cu-Fe Alloys for High Pressure Die-casting, *Mater. Design.*, 2016, **92**, p 151–159. <https://doi.org/10.1016/j.matdes.2015.12.003>
10. Z.H. Yuan, Z.P. Guo and S.M. Xiong, Microstructure Evolution of Modified Die-cast AlSi10MnMg Alloy during Solution Treatment and Its Effect on Mechanical Properties, *Trans. Nonferrous Met. Soc. China*, 2019, **29**, p 919–930. [https://doi.org/10.1016/S1003-6326\(19\)65001-6](https://doi.org/10.1016/S1003-6326(19)65001-6)
11. Q. Cai, C.M.L. Mendis, I.T.H. Chang and Z.Y. Fan, Effect of Short T6 Heat Treatment on the Microstructure and the Mechanical Properties of Newly Developed Die-cast Al-Si-Mg-Mn Alloys, *Mater. Sci. Eng. A*, 2020, **788**, p 139610. <https://doi.org/10.1016/j.msea.2020.139610>
12. R.N. Lumley, R.G. Odonnell, D.R. Gunasegaram and M. Givord, Heat Treatment of High-pressure Die Castings, *Metall. Mater. Trans. A*, 2007, **38**, p 2564–2574. <https://doi.org/10.1007/s11661-007-9285-4>
13. K. Yamamoto, M. Takahashi, Y. Kamikubo, Y. Sugiura, S. Iwasawa, T. Nakata and S. Kamado, Influence of Process Conditions on Microstructures and Mechanical Properties of T5-treated 357 Aluminium Alloys, *J. Alloy. Compd.*, 2020, **834**, p 15533. <https://doi.org/10.1016/j.jallcom.2020.155133>
14. T. Inoue, M. Goto, A. Yamaguchi, T. Otake, A. Kuroda and M. Yoshida, Effect of Pre-aging Conditions on T5 Heat Treatment Behavior of Al-9%Si-0.3%Mg Die-casting Alloy, *J. Jpn. I. Met.*, 2011, **61**(10), p 507–512. <https://doi.org/10.2464/jilm.61.507>
15. T. Ando, S. Onuki, R. Enomoto, M. Tejima, Y. Okada, Aging metallurgy and mechanical properties on Al-Si-Cu-Mg die casting alloy, The Proceedings of the 16th International Aluminum Alloys Conference (ICAA16) 2018
16. R.K. Mishra, G.W. Smith, W.J. Baxter, A.K. Sachdev and V. Franetovic, The Sequence of Precipitation in 339 Aluminum Castings, *J. Mater. Sci.*, 2001, **36**(2), p 461–468. <https://doi.org/10.1023/A:100488831537>
17. T.J. Konno, S. Sasaki and T. Hamaoka, Transmission Electron Microscopic Observation of Precipitates in Age-hardening Die-cast Aluminum Alloys, *J. Jpn. I. Light Met.*, 2016, **66**, p 291–297. <https://doi.org/10.2464/jilm.66.291>
18. T. Ungar, J. Gubicza, P. Hanak and I. Alexandrov, Densities and Character of Dislocations and Size-distribution of Subgrains in Deformed Metals by X-ray Diffraction Profile Analysis, *Mater. Sci. Eng. A*, 2001, **319–321**, p 274–278. [https://doi.org/10.1016/S0921-5093\(01\)01025-5](https://doi.org/10.1016/S0921-5093(01)01025-5)
19. Z. Arechabaleta, P.V. Liempt and J. Sietsma, Quantification of Dislocation Structures from Anelastic Deformation Behavior, *Acta Mater.*, 2016, **115**, p 314–323. <https://doi.org/10.1016/j.actamat.2016.05.040>
20. S.Y. Chen, F.S. Li, K.H. Chen, L.P. Huang and G.S. Peng, Synergic Effect of Hot Deformation Temperature and Pre-straining on Ageing Precipitates and Mechanical Property of 2014 Al Alloy, *Mater. Charact.*, 2020, **167**, p 110510. <https://doi.org/10.1016/j.matchar.2020.110510>
21. I. Zuiko and R. Kaibyshev, Deformation Structures and Strengthening Mechanisms in an Al-Cu Alloy Subjected to Extensive Cold Rolling, *Mater. Sci. Eng. A*, 2017, **702**, p 53–64. <https://doi.org/10.1016/j.msea.2017.07.001>
22. B. Gurrutxaga-Lerma, D.S. Balint, D. Dini and A.P. Sutton, The Mechanisms Governing the Activation of Dislocation Sources in Aluminum at Different Strain Rates, *J. Mech. Phys. Solids*, 2015, **84**, p 273–292. <https://doi.org/10.1016/j.jmps.2015.08.008>
23. H. Okamoto, Phase diagrams for binary alloys, ASM International (2010)
24. S. Ferraro, A. Fabrizi and G. Timelli, Evolution of Sludge Particles in Secondary Die-cast Aluminum Alloys as Function of Fe, Mn and Cr

- Contents, *Mater. Chem. Phys.*, 2015, **153**, p 168–179. <https://doi.org/10.1016/j.matchemphys.2014.12.050>
25. X.X. Dong, H. Youssef, Y.J. Zhang, H.L. Yang, S.H. Wang and S.X. Ji, Advanced Heat Treated Die-cast Aluminium Composites Fabricated by TiB₂ Nanoparticle Implantation, *Mater. Design*, 2020, **186**, p 108372.
 26. Z.H. Yuan, Z.P. Guo and S.M. Xiong, Effect of As-cast Microstructure Heterogeneity on Aging Behavior of a High-pressure Die-cast A380 Alloy, *Mater. Charact.*, 2018, **135**, p 278–286. <https://doi.org/10.1016/j.matchar.2017.11.040>
 27. X.X. Dong, X.S. Huang, L.H. Liu, L.J. He and P.J. Li, A Liquid Aluminum Alloy Electromagnetic Transport Process for High Pressure Die Casting, *J. Mater. Process. Tech.*, 2016, **234**, p 217–227. <https://doi.org/10.1016/j.jmatprotec.2016.03.028>
 28. S. Ji, Y. Wang, D. Watson and Z. Fan, Microstructural Evolution and Solidification Behavior of Al-Mg-Si Alloy in High-pressure Die Casting, *Metall. Mater. Trans. A*, 2013, **44**, p 3185–3197. <https://doi.org/10.1007/s11661-013-1663-5>
 29. A. Hamasaiid, M.S. Dargusch, C.J. Davidson, S. Tovar, T. Loulou, F. Rezai-Aria and G. Dour, Effect of Mold Coating Materials and Thickness on Heat Transfer in Permanent Mold Casting of Aluminum Alloys, *Metall. Mater. Trans. A*, 2007, **38**, p 1303–1316. <https://doi.org/10.1007/s11661-007-9145-2>
 30. K.S. Ghosh, Calorimetric Studies of 2024 Al–Cu–Mg and 2014 Al–Cu–Mg–Si Alloys of Various Tempers, *J. Therm. Anal. Calorim.*, 2019, **136**, p 447–459. <https://doi.org/10.1007/s10973-018-7702-0>
 31. P. Hofer, E. Kaschnitz and P. Schumacher, Distortion and Residual Stress in High-pressure Die Castings: Simulation and Measurements, *JOM*, 2014, **66**, p 1638–1646. <https://doi.org/10.1007/s11837-014-1118-5>
 32. S. Kianfar, E. Aghaie, J. Stroh, D. Sediako and J. Tjong, Residual Stress, Microstructure, and Mechanical Properties Analysis of HPDC Aluminum Engine Block with Cast-in Iron Liners, *Mater. Today Commun.*, 2021, **26**, 101814. <https://doi.org/10.1016/j.mtcomm.2020.101814>
 33. I. Zuiko and R. Kaibyshev, Aging Behavior of an Al-Cu-Mg Alloy, *J. Alloy. Compd.*, 2018, **759**, p 108–119. <https://doi.org/10.1016/j.jallcom.2018.05.053>
 34. L.Y. Ye, Y. Dong, S.D. Liu, H.C. Jiang, D.X. Sun and X.M. Zhang, Effects of Pre-ageing on Microstructure and Mechanical Properties of T916 Treated 2519A Aluminium Alloy, *Met. Mater. Int.*, 2018, **24**, p 1149–1161. <https://doi.org/10.1007/s12540-018-0069-8>
 35. Y. Liu, F. Teng, F.H. Cao, Z.X. Yin, Y. Jiang, S.B. Wang and P.K. Shen, Defective GP-zones and Their Evolution in an Al-Cu-Mg Alloy During High-temperature Aging, *J. Alloy. Compd.*, 2019, **774**, p 988–996. <https://doi.org/10.1016/j.jallcom.2018.10.061>
 36. J.Y. Li, S.Y. Chen, F.S. Li, K.H. Chen and L.P. Huang, Synergy Effect of Si Addition and Pre-straining on Microstructure and Properties of Al–Cu–Mg Alloys with a Medium Cu/Mg Ratio, *Mater. Sci. Eng. A*, 2019, **767**, p 138429. <https://doi.org/10.1016/j.msea.2019.138429>
 37. H. Liu, I. Papadimitriou, F.X. Lin and J. Llorca, precipitation During High Temperature Aging of Al-Cu Alloys: A Multiscale Analysis based on First Principles Calculations, *Acta Mater.*, 2019, **167**, p 121–135. <https://doi.org/10.1016/j.actamat.2019.01.024>
 38. G. Riontino and A. Zanada, Coupled Formation of Hardening Particles on Pre-precipitates in an Al-Cu-Mg-Si 2014 Alloy, *Mater. Lett.*, 1998, **37**, p 241–245. [https://doi.org/10.1016/S0167-577X\(98\)00099-8](https://doi.org/10.1016/S0167-577X(98)00099-8)
 39. P.W. Li, H.Z. Li, X.P. Liang, Y.X. Che, X. Zhan and L. Huang, Effect of Isothermal and Non-isothermal Aging on the Low Cycle Fatigue Behavior of an Al–Cu–Mg–Si Forging Alloy, *Mater. Charact.*, 2018, **144**, p 378–386. <https://doi.org/10.1016/j.matchar.2018.07.027>
 40. Y.Z. Ji, B. Ghaffari, M. Li and L.Q. Chen, Phase-field Modeling of θ' Precipitation Kinetics in 319 Aluminum Alloys, *Comp. Mater. Sci.*, 2018, **151**, p 84–94. <https://doi.org/10.1016/j.commatsci.2018.04.051>
 41. M. Gazizov, G.D. Marioara, J. Friis, S. Wenner, R. Holmestad and R. Kaibyshev, Precipitation Behavior in an Al-Cu-Mg-Si Alloy During Ageing, *Mater. Sci. Eng. A*, 2019, **767**, 138369. <https://doi.org/10.1016/j.msea.2019.138369>
 42. L. Gao, X.Q. Ou, S. Ni, K. Li, Y. Du and M. Song, Effects of θ' Precipitates on the Mechanical Performance and Fracture Behavior of an Al-Cu Alloy Subjected to Overaged Condition, *Mater. Sci. Eng. A*, 2019, **762**, 138091. <https://doi.org/10.1016/j.msea.2019.138091>

Publisher's Note Springer Nature remains neutral with regard to jurisdictional claims in published maps and institutional affiliations.